UC Berkeley
UC Berkeley Previously Published Works

Title

Continuous-flow reactor with superior production rate and stability for CO 2 reduction using semiconductor photocatalysts

Authors

Jung, Hyunju

Kim, Chansol

Yoo, Hae-Wook

et al.

Peer reviewed

Continuous-Flow Reactor with Superior Production Rate and Stability for CO₂ reduction using Semiconductor Photocatalysts

Hyunju Jung[a,b], Chansol Kim[a,b], Hae-Wook Yoo[c], Jei You[d], Jin Seog Kim[d], Aqil Jamal[e], Issam Gereige[e], Joel W. Ager[b,f]*, and Hee-Tae Jung[a,g]*

Semiconductor photocatalyst approaches for solar CO_2 reduction are attractive due to their simplicity but have lagged in efficiency compared to less-integrated photoelectrochemical (PEC) approaches and to electrolysis reactors. We identify poor mass transport and catalyst deactivation as key constraints. To address them, we have developed a continuous-flow photocatalytic reactor system allowing us to control the triple-phase interface on the photocatalyst surface using the liquid and reactant gas flow rates. With the goal of selectively producing CO, the reactor is optimized by controlling the pressure and flow rates of the reactant gas and electrolyte in contact with both sides with the intermediately placed catalyst. In comparison to batch reactors with an immobile photocatalyst bed and gas phase CO_2 or CO_2 purged water, 10–24 times higher production rates are achieved for photocatalysts such as TiO_2, ZnO, C_3N_4, and CdS by simply changing to the designed flow-type photoreactor without any catalyst modification. In addition, CO selectivity (93.2%) and long-term stability (>780 min) using the designed reactor are significantly enhanced compared to using the batch reactors (71.7%, <180 min for reduced 50% activity). We propose that the enhanced mass transport on the photocatalyst surface accelerates the desorption of the initial photolysis product, CO, and prevents the poisoning effect from deactivating photocatalyst activity. This study has the potential to facilitate the utilization of semiconductor-based photocatalytic reactions for achieving superior performance with gaseous reactants.

1 Introduction

Performing the solar light-driven CO₂ reduction reaction (CO₂R) with semiconductor photocatalysts embodies the ideal of artificial photosynthesis due to its simplicity [1,2]. However, photocatalytic CO₂ reduction (PC CO₂R) is severely constrained, owing to its low production rate and poor long-term stability [3,4]. We assert that these limitations are caused not only by high recombination of photoexcited electrons and holes rates, but also by photocatalytic reaction environments with inefficient mass transport and surface poisoning. For example, in a batch reactor with an immobile photocatalyst bed and a gas-phase feed of CO_2 [5,6], the adsorption and desorption of the reactants and products on the photocatalyst surface occur inefficiently because mass transfer occurs only by diffusion in a static system without external flow [7]. Thus, significant quantity of products tends to accumulate on the surface of the photocatalyst, which prevents reactants from occupying the reaction sites. This reduces the low reaction rate and accelerates the degradation of the photocatalyst [8]. On the other hand, in a liquid-phase PC CO₂R batch reactor with the particle photocatalysts dispersed or immobilized in aqueous solution, photoreaction is caused with CO_2 gas saturated with a solvent. Consequently, the activity of the reactant is restricted by its solubility, especially in the case of inert gases like CO_2 and N_2. [9,10]. For these reasons, it is essential to develop a continuous-flow reactor for obtaining highly efficient photocatalytic reactions.

In this study, we take a significant step towards solving limitations imposed by previous batch-type photocatalytic CO₂R reactors. Due to the development of flow reactor systems with an electrocatalytic gas diffusion electrodes (GDEs), the performance of electrocatalytic CO₂R has been significantly enhanced by increasing the mass transport rate in the triple-phase continuous-flow reactors [9,11]., higher Faradaic efficiency even for the same material compared to the H-cell [11–13]. Our new design uses a continuous-flow cell aimed at optimizing conditions at the triple-phase interface region by allowing the circulated liquid electrolyte and pressure-controlled gaseous reactants to flow on the surface of a solid photocatalyst. We hypothesis that in contrast to batch-type photoreactors, in the triple-phase interface reaction of the continuous-flow reactor, there is an abundant and effective supply of gaseous reactants and proton donors in the electrolyte. In addition, the mass transfer rate is further

a. Department of Chemical and Biomolecular Engineering, Korea Advanced Institute of Science and Technology (KAIST), 291 Daehak-ro, Yuseong-gu, Daejeon 34141, South Korea
b. Chemical Sciences Division, Lawrence Berkeley National Laboratory, 1 Cyclotron Road, Berkeley, California 94720, USA
c. The First R&D Institute, Agency for Defense Development, Yuseong-gu, Daejeon 305-600, South Korea
d. Gas Isotope Metrology Team, Korea Research Institute of Standards and Science, Daejeon 34113, South Korea
e. Saudi Aramco, Research and Development Center, Dhahran, 31311 Saudi Arabia.
f. Department of Materials Science and Engineering, University of California Berkeley
g. Korea Advanced Institute of Science and Technology (KAIST) Institute for Nanocentury, Daejeon 34141, South Korea

increased beyond the mass transfer rate caused by diffusion with pressurized flow, owing to the flux applied to both sides of the photocatalyst layer, resulting in a substantial increase in photocatalytic performance.

Results and discussion

Distinguishing features of continuous-flow photocatalytic reactor system

By optimizing the triple phase interface in the photocatalytic reactor, the following are ensured: (i) abundant supply of the highly activated gaseous CO_2 and hydrogen donor (H_2O) in the triple-phase interface reaction and (ii) rapid adsorption and desorption due to the continuous-flow stream (Fig. 1). In the microenvironment on the photocatalyst surface in each reactor environment, the distribution of CO_2 and H_2O molecules is different (Fig. 1(A)). In the liquid-phase batch reactor, the supply of CO_2 molecules is limited, owing to the limited solubility of molecules[9,14]. In the gas-phase batch reactor, the mass transport of reactants and products can be inefficient because there is no external flux and the reaction depends only on diffusion without external convection [15,16]. Both types of batch reactors have a problem in that the microenvironment of the reactant cannot be precisely controlled.

Similar to the electrocatalytic flow cell, in the continuous-flow photocatalytic reactor, CO2 and water molecules are supplied to the reaction sites through the GDL. In addition, by applying pressure to the CO_2 in the flow-type reactor, the solubility of CO_2 in the recycled water increases, as well as the number of CO_2 molecules passing through the GDL and reacting with the catalyst. In addition, the activity of the flow reactor is maintained for a long time because the molecules inducing the poisoning effect are effectively desorbed on the photocatalyst surface, owing to the continuous flows preventing them from re-adsorption on the surface [17] (Fig. 1(B)). Applying flows is particularly effective in photoreactions of photocatalysts where simultaneous oxidation and reduction reactions occur on the surface, as it prevents backward reactions and leads to high reactivity. (Joule 7, 457–468, March 15, 2023, Nature 613, 66–70.)In addition, CO selectivity increases dramatically in the flow reactor. Since the retention time of the adsorbed CO_2 is relatively short in the flow system [18], it is difficult to proceed with further reaction steps for the production of other chemicals such as CH_4 after its reduction to the simplest form of CO [19].

In order to investigate the hypothesis, we designed the reactor components and systems for photocatalytic reactions (Fig. 2(A)). The electrocatalytic flow reactors[11–13] consists of a reactant gas flow plate for the cathode, cathode materials as a conductive GDE, a cathode electrolyte flow plate, an electrolyte membrane, an anode electrolyte flow plate, anode materials as the GDE, and a gas flow plate open to air (Fig. S1, ESI†). In an adaptation of this design, photocatalytic flow reactor is composed of a reactant gas flow plate, a non-conductive gas diffusion layer (GDL), a photocatalyst layer, an electrolyte flow plate, a quartz window plate, and a light source (Fig. 2(B) and Fig. S2, ESI†). All of the reactor plates are composed of steel

material, which is inert to other chemicals and materials during the photochemical reaction.

Control over the flow behaviour, such as the pressure and flow rate of the reactants, is particularly important for accomplishing a high-performance photocatalytic reduction reaction[18,20,21]. There were many difficulties in optimizing the system to elicit a three-phase reaction on the photocatalytic surface, but we found a way, described details in Table S1, ESI†. There were critical factors: First, we constructed the pathway for the passage of light through the water-based transparent electrolyte via a quartz window, where it reaches the photocatalyst surface in order to induce a photocatalytic reaction on a triple-phase interface. Second, we precisely control the reactant gas feed by using the gas pressure regulator, and the flow control valve, meanwhile the flow rate measured by the mass flow meter (MFM) (Fig. S3, ESI†). Third, we built a continuous-flow electrolyte unit. The continuous flow of the electrolyte can avoid the temperature rise caused by photo-illumination on the transparent electrolyte, which can affect the performance of the photocatalytic reaction (Fig. S4, ESI†). To optimize the balance between the flow reactant gas with a specific pressure and flow rate and with a flow electrolyte, we constructed an electrolyte flow unit that continuously flows through a closed circulation pipeline connected at both ends around the photocatalyst layer (Fig. S3, ESI†). This adjustable flow of a pressurized gas enables the reactor to dissolve many reactants in the electrolyte, thus enhancing the production rate of the photocatalytic reaction (Fig. 2(C)).

Then, we fabricated a photocatalytic GDL (Fig. 2(D)). Similar to the GDL in an electrocatalytic flow reactor, small gas molecules can penetrate the hydrophobic GDL through its porous structure, but not hydrophilic molecules such as water-based electrolytes. However, the components and structure of our continuous-flow photoreactor are different from those of an electrocatalytic flow reactor. In an electrocatalytic flow reactor, a conductive carbon cloth or carbon paper is essential in the GDL because electrical overpotential should be applied to the electrocatalyst. However, in the photocatalytic reaction, as the GDL does not need to be a conductor, only hydrophobic porous materials can be used as the GDL without conductive components, which is very beneficial to the long-term stability of our photocatalytic continuous-flow reactor. It is well reported that the conductive carbon layer in the electrocatalytic flow reactor can be damaged during repetitive electrocatalytic reactions, which leads to substantial reduction of catalytic performance[22]. In addition, it can act as a contaminant on the catalyst surface, thereby decreasing the effective reaction area. ~~In fact, the change in the carbon surface from hydrophobic to hydrophilic after a long-term reaction is one of the key limitations of electrocatalytic flow reactor systems [23]~~. Thus, our photocatalytic GDL with a single hydrophobic porous layer should exhibit long-term stability in comparison to the electrocatalytic flow reactor. In addition, in the absence of a conductive carbon layer, the GDL is thinner than that of the electrocatalytic flow reactor, leading to a shorter path length of the reactant gas[22,24]. Consequently, the gas reactants in our flow reactor can be much more efficiently diffused into the photocatalyst layer

and the gaseous product can be diffused out. In this study, we used porous PTFE film with a thickness of 130 μm.

To evaluate the performance of our continuous-flow photocatalytic reactor, we began with commercially available TiO_2 nanoparticles (Degussa P25); this material is widely used in semiconductor photocatalysis due to its wide bandgap, stability (ACS Catal. 2019, 9, 5, 4642–4687) and non-toxic properties. In addition, several other representative CO_2R catalysts including ZnO, C_3N_4, and CdS were also examined.

Photocatalyst performances according to changes in reactor microenvironments.

We optimized the reactor system by controlling the reactant pressure (P), reactant flow rate (q_r), and electrolyte flow rate (q_e) (Fig. 3). The results were determined by averaging at least three identical experiments, and all photocatalytic reactions were conducted at room temperature. To determine the optimum catalyst loading, we examined the production rates under various catalyst loadings (Fig. S5, ESI†). When the catalyst–solvent ratio of the catalyst ink was 1, the most effective catalytic performance and reproducibility were achieved. Hence, this optimized catalyst loading was applied in subsequent experiments. The production rate of the flow reactor was expressed in μmol/g·h through a unit operation which is typically used in photocatalytic studies.

The applied CO_2 gas pressure affected the production rates of CO and CH_4 in this system (Fig. 3(A)). Only the reactant pressure was changed and other operating conditions are fixed (q_r = 10 sccm, and q_e ≈ 16.6 mL/min). As the pressure increased, the overall production rate increased until 1.2 bar. With the further increase in gas pressure, the production rate decreased. Below a pressure of 1.2 bar, the number of CO_2 molecules passing through the GDL is increase in proportion to the pressure [21]. As abundant pressurized gaseous reactants are supplied to the catalyst layer, the triple-phase interface is formed more extensively under atmospheric conditions, greatly improving the production rate. Above a pressure of 1.2 bar, the production rate of CO decreases gradually, while that of CH_4 slightly increased. The decrease in the CO production rate after 1.2 bar might be due to inappropriate triple-phase interface formed by excessive supply of gaseous reactants at the catalyst layer, and the hindered desorption arising from the imbalance between the adsorption and desorption of the reactant and products. As the number of reactants increase due to an increase in pressure, more energy is required for the desorption of the product from the catalyst surface [24,25]. Accordingly, the slight increase in the CH_4 production rate might be due to non-desorbed CO molecules on the catalyst surface. In a slow desorption environment, the probability of further reactions can be increased.

Similarly, we predicted photocatalytic performance is influenced by the reactant gas flow rate, affecting the space time of gaseous reactant (Fig. 3(B)) and product concentration (Fig. S6, ESI†). The space time of the reactant is closely associated with microenvironment near the photocatalyst along with the reaction, adsorption, and desorption of molecules in this reactor. The reactant gas flow rate was controlled by simply tuning a gas flow valve measuring in sccm at 1/8" tubing with all other operating conditions fixed (P ≈ 1.2 bar and q_e ≈ 16.6 mL/min). As the gas flow rate increased, the production rate increased up to q_r ≈ 10 sccm, and with further increase in the gas flow rate, the production rate decreased. With the increase in the gas flow rate, the mass transport of the gas reactants on the catalyst surface increased. It helped desorption of products molecule, especially CO as earlier production of CO_2R, by swiping away equivalized molecules accumulated near catalyst surface. The rate of re-adsorption of CO was significantly lowered and the rate of formation of further reactions like CH_4 was reduced. The highest production rates of CO and CH_4 were 10 sccm and 5 sccm, respectively. This indicated that the reactant CO_2 and the generated CO and CH_4 were efficiently adsorbed, photo-reacted, and desorbed at an appropriate flow rate. In addition, this improved mass transport can sweep the solidified molecules on the photocatalyst surface acting like a poisoning effect. As the flow rate increased above q_r ≈ 10 sccm, the space time of CO_2 molecules was not sufficient for effective adsorption. Since the products of the catalytic reaction was quickly swept away, it leading to reduce overall production rate reducing the probability that the reactants stay on the catalyst. Similarly, in the case of low gas flow rates, effective desorption of generated molecules did not occur due to the long space time, resulting in lower selectivity of methane at q_r < 5 sccm.

The production rate as a function of electrolyte flow rate at the optimum reactant gas pressure and flow rate (P ≈ 1.2 bar and q_r ≈ 10 sccm, respectively) is shown in Fig. 3(C). A water-based electrolyte as proton donor could affect the entire production rate applying hydraulic pressure on the photocatalyst layer by competing gas pressure at the photocatalyst surface. As the electrolyte flow rate increased, the production rate increased by q_e ≈ 16.6 mL/min, and with further increase in the electrolyte flow rate, the production rate decreased. With the increase in the flow rate of a closed water pipeline, the hydraulic pressure against GDL was raised. It contacted with the pressurized reactant gas and formed a three-phase system at the interface where they push each other. Under the constant gas pressure, when the flow rate of the electrolyte was low, it was thought that a relatively low hydraulic pressure was applied to the photocatalyst layer, so that the triple-phase interface exists on the side of the GDL that was slightly further away from the catalyst side. As the flow rate increased, the triple-phase interface gradually moved to the photocatalyst layer, and it can be inferred that the highest production rate was shown at the most appropriate location at water flow rate ~ 16.6 mL/min. At a higher electrolyte flow rate, the higher hydraulic pressure covered the GDL, even if hydrophobic, CO_2 gas molecules could not pass through the GDL, thereby limiting CO_2 supply[26]. A higher CH_4 production rate was observed under low electrolyte flow conditions. This phenomenon is similar to the increased CH_4 production observed for high gas pressure and low gas flow rate conditions

and suggests that low flow rates increase the net residence time, resulting in higher CH_4 production.

The CO_2 production rates of P25 as a function of the reaction time in our flow reactor and gas/liquid batch reactors are shown in Fig. 4. To explore the effects of reactor types on the photocatalytic performance, all reactor conditions and catalyst materials were fixed to the optimized conditions for continuous-flow photocatalytic and batch reactors: a CO_2 pressure of 1.2 bar, a gas flow rate 10 sccm, a water flow rate ~16.6 mL/min. As can be observed, the overall production rate of our continuous-flow reactor was superior to that obtained in conventional batch cells (Fig. 4(A)). As the reaction time increased, the production rate in batch reactors gradually decreased. The production rates of CO and CH_4 at 240 min were 14.5 µmol/g·h and 4.4 in the liquid phase, respectively, and the corresponding production rates in the gas phase were 107 µmol/g·h and 3.6, respectively. However, with the increase in the reaction time, the production rate did not considerably change in our flow reactor. The production rates of CO and CH_4 at 240 min are 318 µmol/g·h and 23.4 µmol/g·h, respectively; these values were ~21 times higher than those obtained in batch cells on average, and ~24 times higher than that obtained in the gas phase batch cell. This demonstrates an order of magnitude increase in performance compared to that reported in previous studies of P25 (Fig. S7 and Table S2, ESI†). Notably, the CO selectivity and long-term stability of photocatalytic reduction reactions were significantly enhanced in our photocatalytic flow reactor. In case of CO selectivity, the average values for the gas and liquid phases in the batch reactor were 66.3% and 77.1%, respectively, at all reaction times. On the other hand, an average CO selectivity of ~93.4% was achieved in our flow reactor. No hydrogen was detected in any experiments. Such high CO selectivity in the flow reactor might be because the flow-type reaction environment strongly affects reaction kinetics [27]. In the flow reactor, the kinetics of the reactants and products were increased on the photocatalyst surface as a result of external factors such as the reactant CO_2 gas flowing under pressure and the cycled flow of water-based electrolyte. Since improved mass transfer in this process provides a favorable environment for desorption on the photocatalyst surface, CO, which is the earliest stage of the CO_2 reduction product, is estimated to be desorbed considerably before the subsequent reaction, i.e., hydrogenation.

Indeed, sustaining long-term photocatalytic performance in photocatalytic reactions is a challenge. Fig. 4(B) shows the ratio of the total production rate compared to the initial value (C/C_0) of P25 during CO_2R in each reactor. For gas/liquid batch reactors, the production rates rapidly decreased by 50% from the initial activity after 180 min. Then, after 480 min, catalyst performance decreased gradually by less than 10% of the initial production rate, and only 5% of the performance remained after 720 min. This deactivation is an intrinsic problem of photocatalysts, and has been well reported to be due to the immobilized reactants and products or carbon on the photocatalytic surfaces[28]. Thus far, the photocatalytic activity of a majority of conventional TiO_2-based photocatalysts decreased in just a few hours, and their stability did not last long even

when a cocatalyst or conductor is introduced [29]. On the other hand, it was observed that the initial CO activity of the flow reactor was well maintained without significant loss of performance even after 720 min, with $C/C_0 \approx 1.2$. This enhancement can be attributed to the improved mass transfer flow leading to the desorption of reactants or products immobilized on the photocatalyst surface, while avoiding a reduction of the actual reaction area. We have observed that there is no significant change in the C/C_0 value even after more than 100 hours (Fig. S8, ESI†). Consequently, simply changing a batch-type reactor into a continuous-flow photocatalytic reactor system dramatically increased the performance and durability of photocatalysts.

To ensure that the products produced by photoreaction in our flow reactor do not originate from impurities in the system components, blank reaction tests were carried out under the same reaction conditions: i) without light irradiation, ii) with light irradiation of N_2 and H_2O streams in the absence of CO_2, iii) with light irradiation in the presence of CO_2 using a bare PTFE film without photocatalysts, and iv) with light irradiation in the presence of CO_2 with P25 as the photocatalyst (Fig. S9, ESI†). Out of all conditions, the GC signal for CO could be detected only with light irradiation in the presence of CO_2 with P25. Additionally, isotope labelling tests were carried out using gas chromatography–mass spectrometry (GC–MS) (Fig. S10, ESI†).We conclude that the CO_2 fed to the cell is the source of all carbon-containing products in this work.

We also measured the O_2 production rate (Fig. S11, ESI†), which was ~60 µmol/g·h with the optimized condition: $P = 1.2$ bar, $q_r = 10$ sccm q_e ~16.6 mL/min. This value was lower than expected for stoichiometric CO and CH_4 formation (e/h > 1) where e and h mean photo-generated electrons and holes respectively from a photocatalyst. Other photocatalytic studies have also observed e/h > 1 [ref]. While we do not know the precise reason that less O_2 is observed than expected, it is possible that it is due to desorption of OH intermediates and peroxides before water formed into O_2.

Versatility of the continuous-flow photocatalytic reactor design

The promising features of our flow reactor apply to other photocatalytic materials. Other semiconductor-based photocatalysts for CO_2R were considered. TiO_2 and ZnO are typically used as ultraviolet (UV) photocatalysts for CO_2R, absorbing UV light with a wide bandgap. In addition, C_3N_4 and CdS are representative photocatalysts for CO_2R, owing to their high reactivity under visible-light irradiation. In addition, we tested a composite photocatalyst of Pt decorated with P25 nanoparticles (Pt-P25), which is well known to exhibit good photocatalytic performance, owing to the high conductivity of Pt resulting from the effective separation of the photoexcited electrons from the photocatalyst and participation in the reaction before charge recombination[31,32]. The Pt-P25 were prepared and checked its well-formed in Fig. S12, ESI†.

Fig. 5 shows the CO_2R production rates of various CO_2R photocatalysts including TiO2 (P25), ZnO, C_3N_4, and CdS in the flow reactor and gas-phase batch reactors. The photocatalysts

were spray-coated on a PTFE film at the same loading amount and we evaluated CO_2 photoreduction reactions in the flow and gas-phase batch reactors under the same reaction conditions (reaction time: 240 min; P: 1.2 bar; light intensity: 300 mW/cm^2 from a 300-W Xe lamp for UV photocatalysts, with a 300 nm cut-off filter for visible irradiation in case of visible photocatalysts; cell volume for the batch cell: 50 mL; q_r: 10 sccm; and q_e: 16.6 mL/min).

In the case of UV-reactive photocatalysts (P25, Pt-P25, and ZnO), the production rates are significantly improved in the flow reactor, exhibiting production rate enhancements of 24, 15, and 23.3 times, respectively, compared with those observed in the batch cell. Interestingly, the CO selectivity of all photocatalysts is significantly enhanced in our flow reactor. For Pt-P25, the CO selectivity increases from 89.0% in the batch reactor to 97.1% in the flow reactor. For P25, the CO selectivity increases from 87.3% to 98.8%. In addition, we investigated the photocatalytic performance of visible-light-reactive photocatalysts (C_3N_4 and CdS) in the flow and batch reactors. The production rates for the photocatalysts in the flow reactor are ~9.6 times and ~1600 times higher than those in the batch reactor. For C3N4, the CO selectivity increased from 73.6% in the batch reactor to 93.6% in the flow reactor. For CdS, it increased from 74.3% to 91.7%. This is because, as described above, gas and water flowing through the GDL facilitate the desorption of molecules while simultaneously accelerating the mass transfer of the catalyst. Then, CO, which is the initial reactant of CO_2R, is produced more selectively than batch reactors. Therefore, the flow reactor developed herein can be universally applied to photocatalysts under various compositions and conditions, and it can significantly increase the photocatalytic performance, including efficiency, selectivity, and long-term stability.

Conclusions

Our newly designed continuous flow type reactor allows for significant increases in selective activity for photocatalytic CO_2 reduction. By using a gas-diffusion electrode, access of the gas phase reactant to the catalytic triple phase boundary and removal of products from the catalyst surface can be separately optimized. Using P25 TiO_2, optimization of the microenvironment in this way has resulted in a remarkable ~24 fold increase in production rate, a 93.2% improvement in CO selectivity, and 12 hour stability without exchange of any media when compared with standard batch reactors (100 hours stability is achieved with exchange of the liquid electrolyte). Similar increases (at least one order of magnitude) are observed with other CO2R photocatalysts: ZnO, C_3N_4, and CdS. Clearly, in addition to charge recombination, control of gas and liquid mass transport and of the resulting desorption of products are critical factors in the design of efficient photocatalysts for CO_2 reduction or for other photocatalytic reactions which rely on triple phase boundary. Finally, this work shows the activity of many previously studied CO_2R photocatalysts should be re-evaluated, as their performance could have been limited by inadequate mass transport.

Author Contributions

H. J. and H-T. J. conceived the idea and supervised the project. H. J. performed photocatalytic experiments and measurements and carried out data analysis. C.K. supervised the cell assembly and modification. H.-W. Y. supervised the system settings and measurements. J.Y and J. S. K proceed with isotope analysis. H-T. J and J.A. supervised the manuscript.

## Conflicts of interest

There are no conflicts to declare.

References

1   D. Kim, K. K. Sakimoto, D. Hong and P. Yang, Angewandte Chemie - International Edition, 2015, 54, 3259–3266.
2   W. J. Ong, L. L. Tan, Y. H. Ng, S. T. Yong and S. P. Chai, Chem Rev, 2016, 116, 7159–7329.
3   S. N. Habisreutinger, L. Schmidt-Mende and J. K. Stolarczyk, Angewandte Chemie - International Edition, 2013, 52, 7372–7408.
4   O. K. Varghese, M. Paulose, T. J. LaTempa and C. A. Grimes, Nano Lett., 2009, 9, 731–737.
5   I. Shown, S. Samireddi, Y. C. Chang, R. Putikam, P. H. Chang, A. Sabbah, F. Y. Fu, W. F. Chen, C. I. Wu, T. Y. Yu, P. W. Chung, M. C. Lin, L. C. Chen and K. H. Chen, Nat Commun, , DOI:10.1038/s41467-017-02547-4.
6   X. Li, Y. Sun, J. Xu, Y. Shao, J. Wu, X. Xu, Y. Pan, H. Ju, J. Zhu and Y. Xie, Nat Energy, 2019, 4, 690–699.
7   D. M. Fabian, S. Hu, N. Singh, F. A. Houle, T. Hisatomi, K. Domen, F. E. Osterloh and S. Ardo, Energy Environ Sci, 2015, 8, 2825–2850.
8   S. Navalón, A. Dhakshinamoorthy, M. Álvaro and H. Garcia, ChemSusChem, 2013, 6, 562–577.
9   D. M. Weekes, D. A. Salvatore, A. Reyes, A. Huang and C. P. Berlinguette, Acc Chem Res, 2018, 51, 910–918.
10 P. Lobaccaro, M. R. Singh, E. L. Clark, Y. Kwon, A. T. Bell and J. W. Ager, Physical Chemistry Chemical Physics, 2016, 18, 26777–26785.
11 D. Higgins, C. Hahn, C. Xiang, T. F. Jaramillo and A. Z. Weber, ACS Energy Lett, 2019, 4, 317–324.
12 J. R. C. Junqueira, P. B. O'Mara, P. Wilde, S. Dieckhöfer, T. M. Benedetti, C. Andronescu, R. D. Tilley, J. J. Gooding and W. Schuhmann, ChemElectroChem, 2021, 8, 4848–4853.
13 G. L. de Gregorio, T. Burdyny, A. Loiudice, P. Iyengar, W. A. Smith and R. Buonsanti, ACS Catal, 2020, 10, 4854–4862.
14 Q. Chen and J. an Meng, Int J Heat Mass Transf, 2008, 51, 2863–2870.

15 S. Wang, M. Xu, T. Peng, C. Zhang, T. Li, I. Hussain, J. Wang and B. Tan, Nat Commun, , DOI:10.1038/s41467-019-08651-x.

16 L. Shi, T. Wang, H. Zhang, K. Chang and J. Ye, Adv Funct Mater, 2015, 25, 5360–5367.

17 M. Dilla, R. Schlögl and J. Strunk, ChemCatChem, 2017, 9, 696–704.

18 S. Ali, M. C. Flores, A. Razzaq, S. Sorcar, C. B. Hiragond, H. R. Kim, Y. H. Park, Y. Hwang, H. S. Kim, H. Kim, E. H. Gong, J. Lee, D. Kim and S. il In, Catalysts, 2019, 9, 1–26.

19 C. Bie, H. Yu, B. Cheng, W. Ho, J. Fan and J. Yu, Advanced Materials, 2021, 33, 1–26.

20 T. Mizuno, K. Adachi, K. Ohta and A. Saji, J Photochem Photobiol A Chem, 1996, 98, 87–90.

21 M. Ali, F. Zhou, K. Chen, C. Kotzur, C. Xiao, L. Bourgeois, X. Zhang and D. R. MacFarlane, Nat Commun, 2016, 7, 1–5.

22 C. T. Dinh, T. Burdyny, G. Kibria, A. Seifitokaldani, C. M. Gabardo, F. Pelayo García De Arquer, A. Kiani, J. P. Edwards, P. de Luna, O. S. Bushuyev, C. Zou, R. Quintero-Bermudez, Pang, D. Sinton and E. H. Sargent, Science (1979), 2018, 360, 783–787.

23 M. K. Kovalev, H. Ren, M. Zakir Muhamad, J. W. Ager and A. A. Lapkin, ACS Energy Lett, 2022, 7, 599–601.

24 Z. Xing, L. Hu, D. S. Ripatti, X. Hu and X. Feng, Nat Commun, 2021, 12, 1–11.

25 Q. Wang, T. Hisatomi, Q. Jia, H. Tokudome, M. Zhong, C. Wang, Z. Pan, T. Takata, M. Nakabayashi, N. Shibata, Y. Li, I. D. Sharp, A. Kudo, T. Yamada and K. Domen, Nat Mater, 2016, 15, 611–615.

26 B. de Mot, J. Hereijgers, M. Duarte and T. Breugelmans, Chemical Engineering Journal, 2019, 378, 1–8.

27 X. Kong, C. Wang, Z. Xu, Y. Zhong, Y. Liu, L. Qin, J. Zeng and Z. Geng, Nano Lett, 2022, 22, 8000–8007.

28 D. Panayotov, P. Kondratyuk and J. T. Yates, Langmuir, 2004, 20, 3674–3678.

29 F. He, U. Muliane, S. Weon and W. Choi, Appl Catal B, 2020, 275, 119145.

30 U. Kang, S. H. Yoon, D. S. Han and H. Park, ACS Energy Lett, 2019, 4, 2075–2080.

31 Q. Zhai, S. Xie, W. Fan, Q. Zhang, Y. Wang, W. Deng and Y. Wang, Angewandte Chemie, 2013, 125, 5888–5891.

32 B. Fang, A. Bonakdarpour, K. Reilly, Y. Xing, F. Taghipour and D. P. Wilkinson, ACS Appl Mater Interfaces, 2014, 6, 15488–15498.

33 J. Taing, M. H. Cheng and J. C. Hemminger, ACS Nano, 2011, 5, 6325–6333.

34 Y. Li, Y. Cai, X. Chen, X. Pan, M. Yang and Z. Yi, RSC Adv, 2016, 6, 2760–2767.
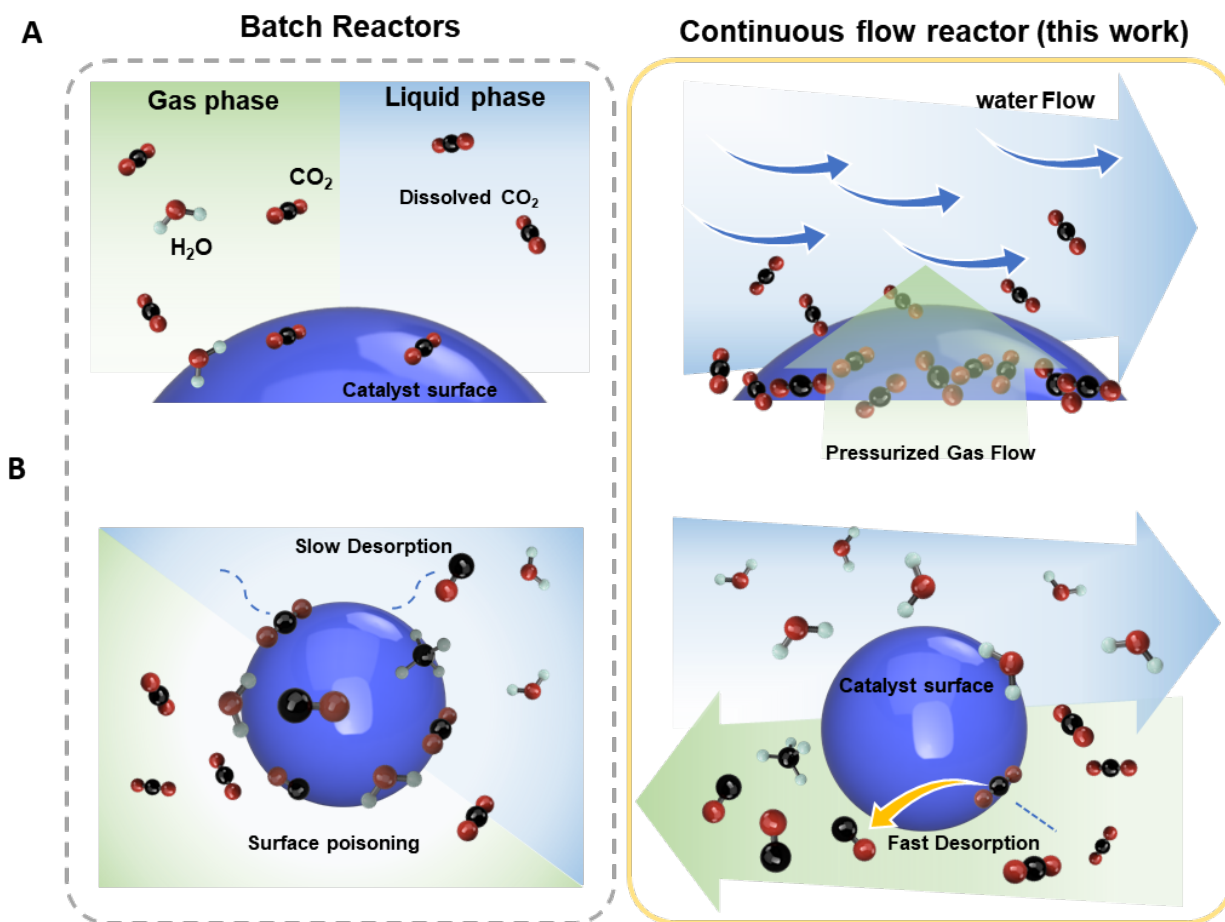
**Fig. 1 Illustration of microenvironments of batch reactors and continuous flow reactor.** (**A**) distribution of CO_2 and H_2O molecules near photocatalyst in gas and liquid phase batch reactors (left), and the continuous flow reactor (right) used in this work. (**B**) Illustration of molecular behavior on the surface of a photocatalyst according to the reaction environment: batch reactor (left) has poor mass transfer of reactant intermediate species which can lead surface poisoning; the continuous flow reactor (right) has improved mass transfer for desorption of products and optimal activities for the reactants.
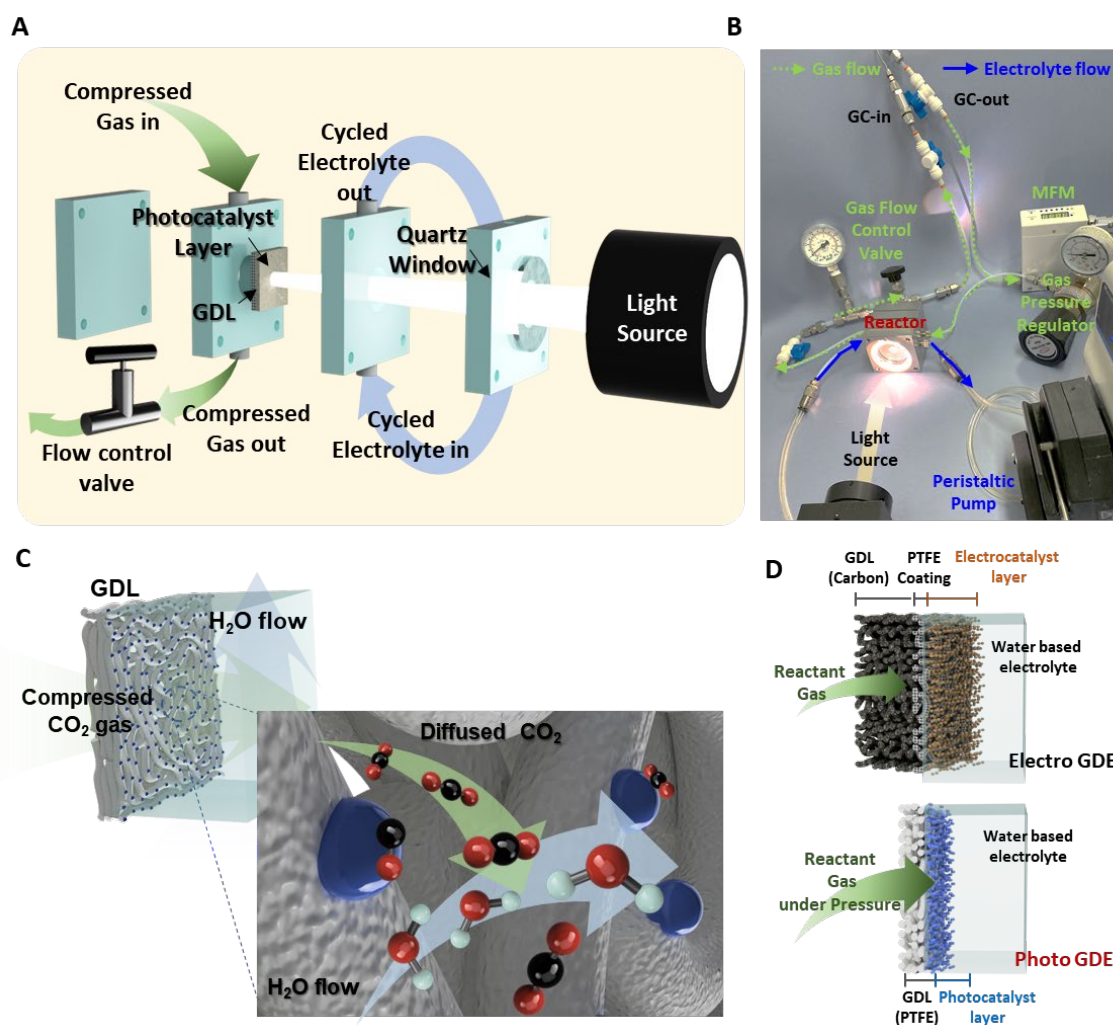
Fig. 2. Implementation of the GDE design to the photocatalytic reactor system. (**A**) Magnified diagram of the continuous-flow photocatalytic reactor. (**B**) Photograph of the flow reactor system in operation. (**C**) Diagram of a three-phase reaction on the photocatalytic GDE structure. (**D**) Diagram of structure of the GDE in an electrocatalytic flow reactor (upper image) and in a continuous-flow photocatalytic reactor (bottom image).
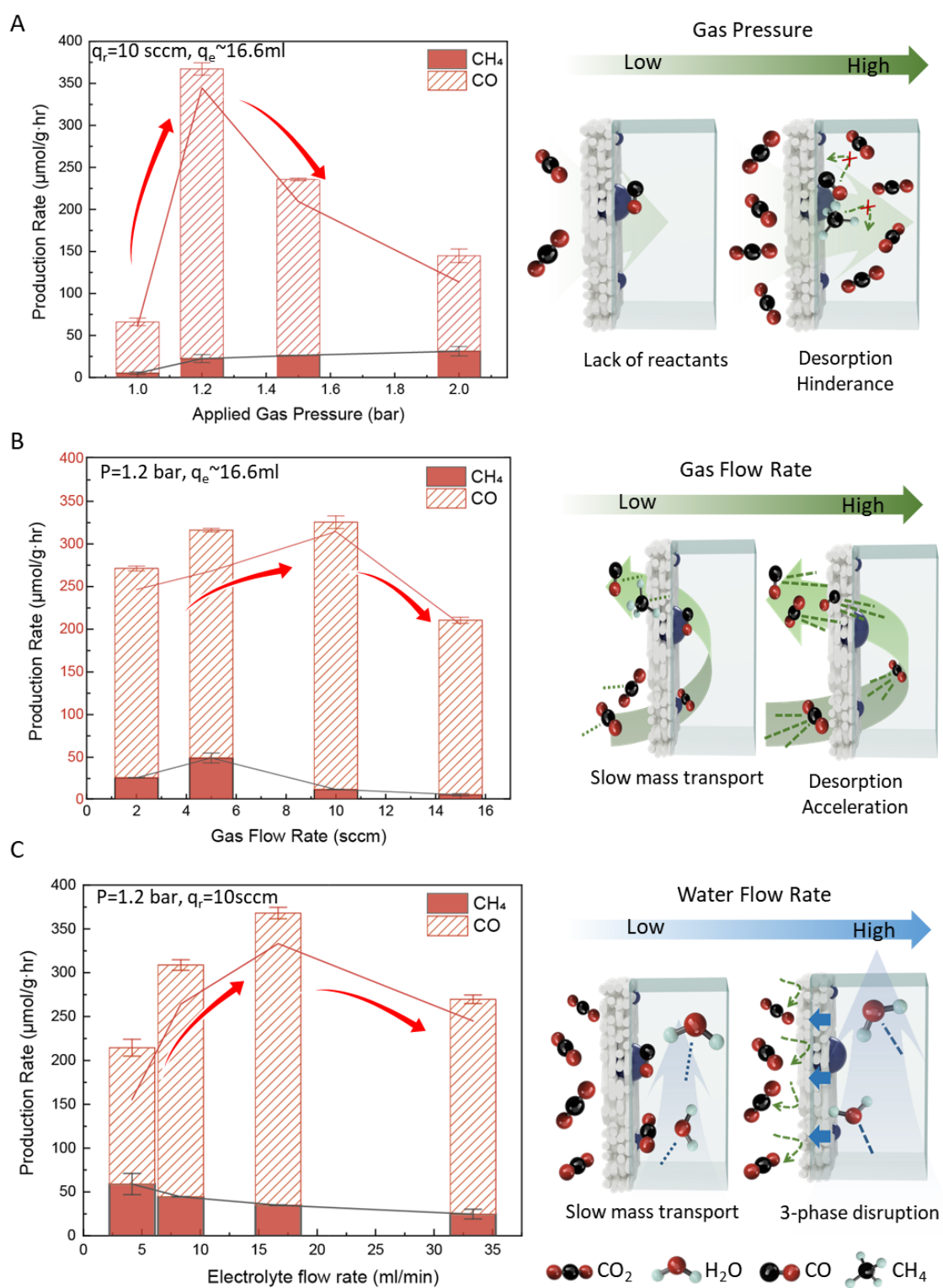
Fig. 3. Effects of various factors on the flow-type reactor system. (**A**) Effect of applied CO_2 gas pressure. (**B**) Effect of gas flow rate on the production rate. (**C**) Effects of the cycled electrolyte flow rate on the production rates of CO and CH_4. On the right of each graph, diagrams show the catalyst surface at both the low and high ends. Error bars in (A)-(C) are standard deviations from 3 replicate experiments.
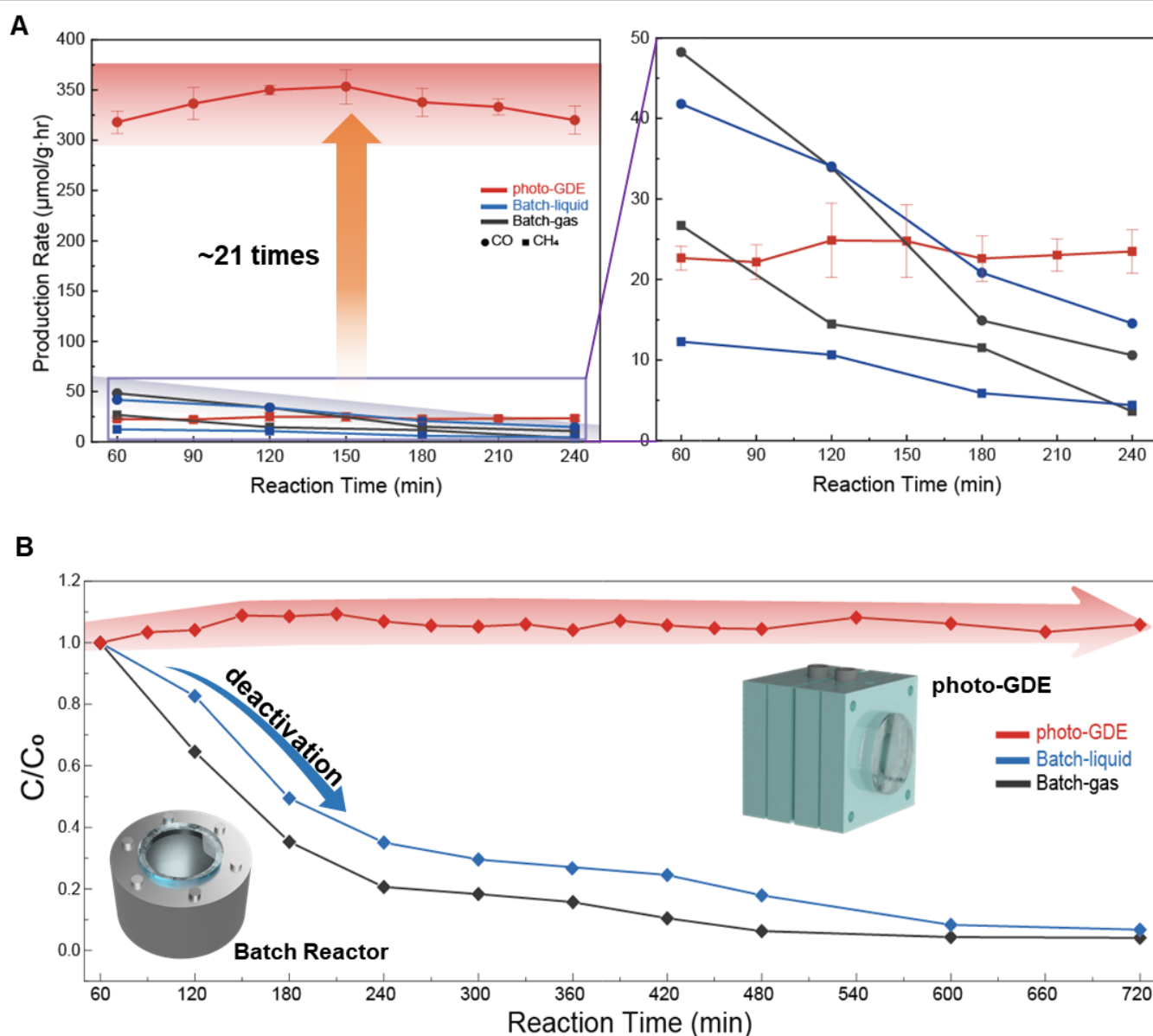
Fig. 4. CO$_2$ conversion performance of P25 in the flow-type and batch-type reactors. (**A**) Production rates of P25 measured in the flow-type photocatalytic reactor (●: CO and ■: CH$_4$) and gas (●: CO and ■: CH$_4$)/liquid (●: CO and ■: CH$_4$) batch reactors. The graph on the right is a magnified image of the low production rate. (**B**) Ratio of the total production rate to the initial value (C/C$_0$) measured in the flow-type photocatalytic reactor (◆), liquid-phase batch cell (◆), and gas-phase batch cell (◆). Error bars in (A) are standard deviations from 3 replicate experiments.
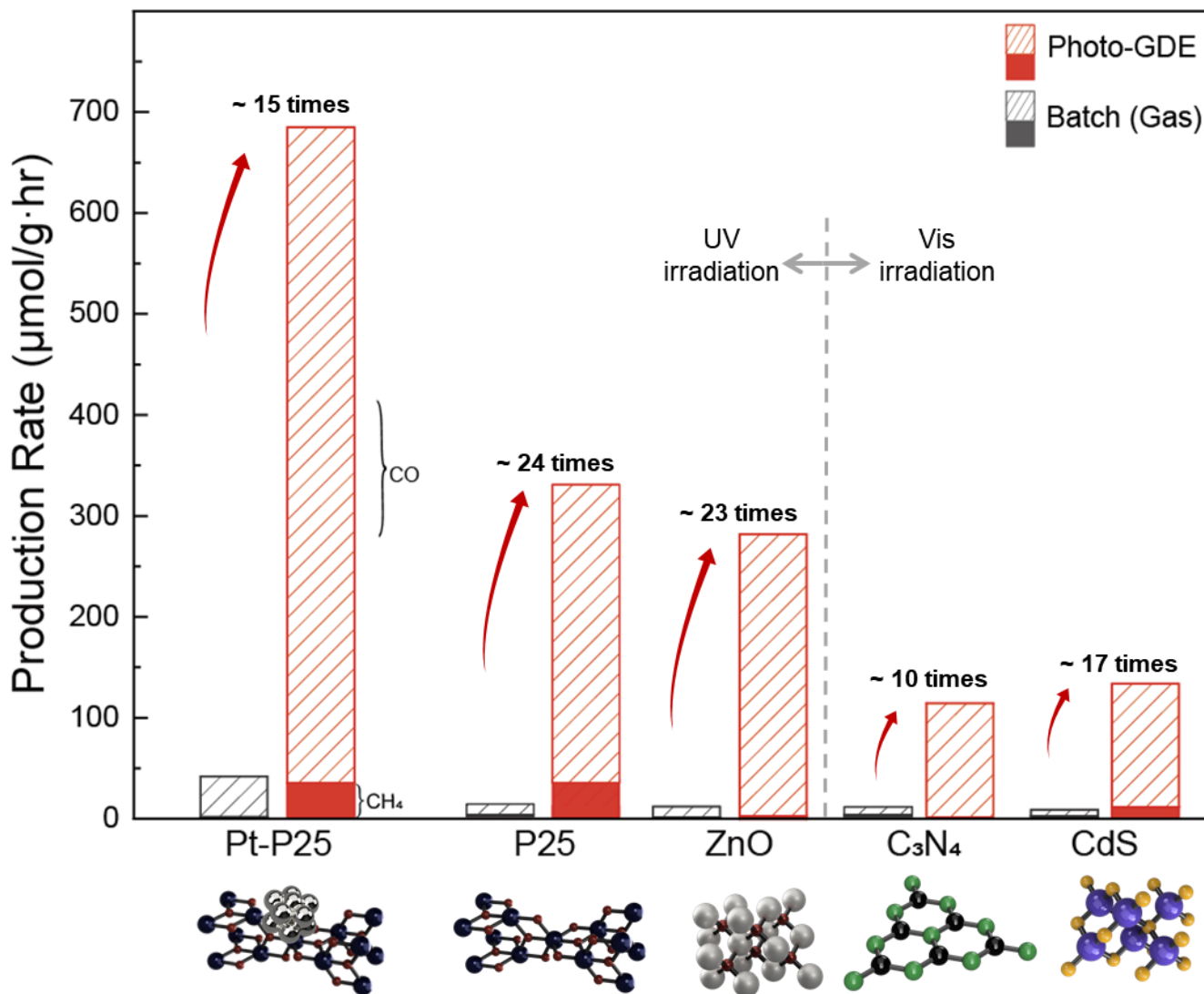
Fig. 5. **CO₂ conversion performance of various photocatalysts.** CO_2 reduction to CO (dashed box) and CH_4 (solid box) in a flow reactor (red) and a gas-phase batch reactor (black) with representative photocatalyst base materials Pt-decorated P25 (Pt-P25), P25, ZnO, C_3N_4, and CdS, with each molecular model depicted at the bottom. In the case of P25, it is depicted as anatase TiO_2.